Bayesian Inversion of Seismic and Electromagnetic Data for Marine Gas Reservoir Characterization Using Multi-chain Markov Chain Monte Carlo Sampling

Received: 9/1/2016

Accepted:

Huiying Ren[1,*], Jaideep Ray[2], Zhangshuan Hou[1], Maoyi Huang[1], Jie Bao[1], Laura Swiler[3]

1: Pacific Northwest National Laboratory, Richland WA, USA

2: Sandia National Laboratories, Livermore CA, USA

3: Sandia National Laboratories, Albuquerque, NM, USA

*: Corresponding Author: Pacific Northwest National Laboratory, PO Box 999, Richland, WA 99352, Tel: 1-509-372-4088, Fax: 1-509-372-6089, Huiying.Ren@pnnl.gov

Abstract

In this study we developed an efficient Bayesian inversion framework for interpreting marine seismic Amplitude Versus Angle and Controlled-Source Electromagnetic data for marine reservoir characterization. The framework uses a multi-chain Markov-chain Monte Carlo sampler, which is a hybrid of DiffeRential Evolution Adaptive Metropolis and Adaptive Metropolis samplers. The inversion framework is tested by estimating reservoir-fluid saturations and porosity based on marine seismic and Controlled-Source Electromagnetic data. The multi-chain Markov-chain Monte Carlo is scalable in terms of the number of chains, and is useful for computationally demanding Bayesian model calibration in scientific and engineering problems. As a demonstration, the approach is used to efficiently and accurately estimate the porosity and saturations in a

representative layered synthetic reservoir. The results indicate that the seismic Amplitude Versus Angle and Controlled-Source Electromagnetic joint inversion provides better estimation of reservoir saturations than the seismic Amplitude Versus Angle only inversion, especially for the parameters in deep layers. The performance of the inversion approach for various levels of noise in observational data was evaluated – reasonable estimates can be obtained with noise levels up to 25%. Sampling efficiency due to the use of multiple chains was also checked and was found to have almost linear scalability.

Keywords: Seismic Amplitude Versus Angle; Controlled-Source Electromagnetic; joint inversion; Bayesian; Multi-chain Markov-chain Monte Carlo

1 Introduction

Successful marine gas reservoir characterization requires accurate estimation of reservoir properties such as porosity and fluid/gas saturations, and the quantification of errors/uncertainties in these estimates. Controlled-Source Electromagnetic (CSEM) data are known to be sensitive to the presence of hydrocarbons – as shown in Archie's law (Archie, 1942), the electrical resistivity of reservoir rocks is highly sensitive to gas saturation through the link to water saturation. Such a dependence of bulk resistivity on gas saturation makes it possible to discriminate between economic and non-economic gas saturations. However, the CSEM data are insensitive to geological structural details, which makes standalone CSEM inversion challenging to interpret. Seismic data, on the other hand, provide detailed structural information and can help resolve rock properties such as porosity, but cannot distinguish fluid properties given the inadequate contrast in density and seismic velocities. Since seismic velocity and density have low sensitivity to

variations in gas saturation (Castagna and Backus, 1993; D e¸ bski and Tarantola, 1995; Plessix and Bork, 2000), both fluid and pressure changes have approximately the same degree of impact on the seismic Amplitude Versus Angle (AVA) data according to Gassmann's equations(Gassmann, 1951). The two types of data (seismic AVA and CSEM) can therefore be used as supplementary information to each other to provide adequate constraints on reservoir properties. There have been successful applications of joint inversion of seismic AVA and CSEM data for characterizing marine reservoirs e.g.,((Aki and Richards, 1980) (Chen et al., 2007) (Du and MacGregor, 2010) (Fliedner et al., 2011) (Hou et al., 2006) (Lang and Grana, 2015)).

Although joint inversion of seismic AVA and CSEM data can provide better estimates of gas saturation and porosity than inversion of individual data sets (Chen et al., 2004; Chen et al., 2007; Hou et al., 2006), the integration of two types of data can be challenging due to the high dimensionality of the unknown parameter space. Consequently, parameter estimates and their uncertainties may vary significantly given the choice of inversion approaches (e.g., deterministic versus stochastic), designs of objective and likelihood functions and the transformation and weighting of observational data.

In typical geophysical characterization, the existence of noise and the inadequacy (e.g., spatial and temporal coverage and resolution) of the data imply that the problem is ill constrained and therefore, geophysical characterization is a good target for statistical inference. Since there is usually an infinite number of models that can fit the data, it is useful to employ stochastic approaches (e.g., Bayesian), where unknowns are inferred in the form of a posterior probability density function (PDF), thus automatically quantifying the uncertainty in the estimates of the

unknowns. The estimation problem is posed as a statistical inverse problem, which provides an expression for the posterior density (alternatively, the joint PDF of the unknowns of interest). The PDF is realized by drawing samples using a method such as Markov chain Monte Carlo (MCMC). MCMC (Liang et al., 2011) methods describe a random walk in the parameter space. Each step in the walk is evaluated by running a forward model to gauge the quality of a new parameter proposal (alternatively, a proposed step in the random walk). Most proposed steps are rejected, making MCMC very expensive, since a sufficient number of samples need to be taken to recover the PDF. To reduce computational time, multi-chain (i.e., parallel) MCMC methods have been developed. Our MCMC procedure starts with 4 chains running DREAM (DiffeRential Evolution Adaptive Metropolis; (Vrugt et al., 2009))When a sufficient number of samples have been collected by DREAM to make a useful proposal distribution, the MCMC method transitions to a parallel (4 chains) AM (Adaptive Metropolis;(Haario et al., 2006)), implemented in a manner identical to Solonen's method (Solonen et al., 2012).

In our paper, we considered a five-layer reservoir model, similar to the synthetic model setup in (Hou et al., 2006), to demonstrate the accuracy and efficiency of the newly developed multi-chain MCMC-Bayesian approach. The unknowns include gas saturation and porosity in each layer in the reservoir. We also investigated the performance of the proposed approach under different levels of noise in both seismic AVA and CSEM observational data, and evaluated the efficiency and scalability of the multi-chain MCMC.

The paper is organized as follows. Section 2 introduces the methodology, followed by the results and discussions in Section 3. Concluding remarks are presented in Section 4.

2 Methodology

2.1 Seismic AVA and CSEM Modeling

In seismic modeling, the reservoir variables of interest are porosity ($\boldsymbol{\varphi}$), water ($\mathbf{S_w}$) and gas saturation ($\mathbf{S_g}$) within the reservoir. The Zoeppritz equation (Aki and Richards, 1980)was used to model the angle-dependent reflectivity, which is convolved with the compressional wave reflection coefficient to form the calculated seismic AVA responses (Shuey, 1985). ρ, V_p and V_s (density, compressional and shear wave velocities) of the reservoir are calculated from water and gas saturation and porosity using a rock-physics model as described by (Dvorkin and Nur, 1996) and (Hoversten et al., 2003)The model parameters are adopted from(Chen et al., 2007) . The bulk and shear moduli and density are assumed known, and in practice can be obtained from nearby well logs or can be included in the unknown parameters to be inverted.

CSEM data are the amplitude and phases of the recorded electrical field as a function of frequency and transmitter-receiver offsets. This data is gathered at 21 receivers located on the seafloor. CSEM data are the responses to the electrical conductivity of the entire half-space, which includes the seawater ($\boldsymbol{\sigma_s}$), the overburden ($\boldsymbol{\sigma_o}$) above the reservoir, the reservoir and the bedrock beneath the reservoir. For the EM forward model, we applied an integral-equation solution for the electric field from an electric-dipole source within a layered medium (Ward and Hohmann, 1988). The sensitivity of electrical resistivity of reservoir rocks linked to water saturation can be modeled by Archie's law (Archie, 1942).

We assumed that the rock-physics models and Archie's law (which relate seismic velocity density and electrical conductivity) are given and exact. The pore pressure was also assumed to be constant. We also assume the effects of multiple reflections and waveform spreading can be neglected in seismic AVA data. The rock-physics model and Archie's law parameters used in our inversion are listed in Table1.

2.2 Bayesian Framework

We first explain the basic formulation of a Bayesian inverse problem and then adapt it for our problem. Consider a model $\mathbf{Y} = \mathcal{M}(\theta)$, which is driven by parameters θ. Consider, too, that we have observations $\mathbf{Y}^{(obs)} = \{y_j^{(obs)}\}$, j = 1 … M, of **Y**. So $\mathbf{Y}^{(obs)}$ is a vector of M observations. We seek to infer θ from $Y^{(obs)}$. We relate the model predictions to the observations using an error model, in our case, a Gaussian with zero mean

$$\mathbf{Y}^{(obs)} = \mathcal{M}(\theta) + \boldsymbol{\varepsilon}, \boldsymbol{\varepsilon} = \{\varepsilon_i\}, \varepsilon_i \sim \mathcal{N}(0, \sigma^2). \quad (1)$$

Here ε_i are the "errors" or the model-data mismatch. It is a composite of the measurement error and, in real-data inversion, the structural error. The structural error is the mismatch between observations and model predictions due to "missing physics" i.e., model approximations. Under this formulation, the likelihood of observing a single observation $y_j^{(obs)}$, for a given value of θ, is

$$f\left(y_j^{(obs)}\middle|\theta\right) = \frac{1}{(2\pi)^{1/2}\sigma}\exp\left(-\frac{\varepsilon_j^2}{2\sigma^2}\right) = \frac{1}{(2\pi)^{1/2}\sigma}\exp\left(-\frac{\left(y_j^{(obs)} - \mathcal{M}^j(\theta)\right)^2}{2\sigma^2}\right) \quad (2)$$

where $\mathcal{M}^j(\theta)$ is the j^{th} component of the model prediction. Consequently, the likelihood $f\left(\mathbf{Y}^{(obs)}\middle|\theta\right)$ of observing the data $\mathbf{Y}^{(obs)}$ for any given value of θ, is given by

$$f(\mathbf{Y}^{(\text{obs})} \mid \theta) = \prod_{j}^{M} f\left(y_j^{(obs)} | \theta\right) = \frac{1}{(2\pi)^{\frac{M}{2}} \sigma^M} \exp\left[- \frac{\left\| \mathbf{Y}^{(\text{obs})} - \mathcal{M}(\theta) \right\|_2^2}{2\sigma^2} \right] \tag{3}$$

where $\|\cdots\|_2$ is the L_2 norm. If one has two types of observations $\mathbf{Y_1}^{(\text{obs})}$ and $\mathbf{Y_2}^{(\text{obs})}$, of lengths M_1 and M_2, corresponding to two models driven by two different sets of parameters $\mathcal{M}(\theta_1)$ and $\mathcal{M}(\theta_2)$, the likelihood expression is written as

$$f(\mathbf{Y_1}^{(\text{obs})}, \mathbf{Y_2}^{(\text{obs})} \mid \theta_1, \theta_2) = \frac{1}{(2\pi)^{\frac{M_1+M_2}{2}} \sigma_1^{M_1} \sigma_2^{M_2}} \exp\left[- \frac{w_1 \left\| \mathbf{Y_1}^{(\text{obs})} - \mathcal{M}_1(\theta_1) \right\|_2^2}{2{\sigma_1}^2 M_1} - \frac{w_2 \left\| \mathbf{Y_2}^{(\text{obs})} - \mathcal{M}_2(\theta_2) \right\|_2^2}{2{\sigma_2}^2 M_2} \right] \tag{4}$$

Here, we have adjusted for the unequal number of observations of two types, as well as the fact that their error models may have different σ. We have also accommodated the fact that the two data streams $\mathbf{Y_1}^{(\text{obs})}$ and $\mathbf{Y_2}^{(\text{obs})}$ could be differentially weighted with weights w_1 and w_2. Given probability distributions that express our prior belief in the distributions of the parameter i.e., $\pi(\theta)$, we can use Bayes' formula to write out an expression for the posterior distribution

$$f\left(\theta \mid \mathbf{Y}^{(\text{obs})}\right) \propto f(\mathbf{Y}^{(\text{obs})} | \theta)\, \pi(\theta). \tag{5}$$

Extending this formula for the posterior distribution when we have two observational datasets $\mathbf{Y_1}^{(\text{obs})}$ and $\mathbf{Y_2}^{(\text{obs})}$ is straightforward. Note that in general $f\left(\theta | \mathbf{Y}^{(obs)}\right)$ is a general probability density (and not an analytical one like log-normal or Gamma), and does not have a closed form expression. One has to draw samples from it, using a method such as Markov chain Monte Carlo, and histogram the samples to visualize it. We now adapt this formulation to our inverse problem that uses both seismic and EM data.

The estimation problem is posed with the assistance of two forward models for seismic (elastic wave) transport and electromagnetic wave propagation. The unknowns being estimated are gas saturations $\boldsymbol{S}_g = \{S_{g,i}\}$ and porosities $\boldsymbol{\varphi} = \{\varphi_i\}$, $i = 1 \cdots 5$, in the 5 layers of the target zone (see Fig. 1). The first model, $\boldsymbol{M}^{AVA}$, uses wave speeds (V_p, V_s) and density (ρ) in the overburden, bedrock and target zone (see Fig. 1) to predict the seismic AVA data. The wave speeds and density in the bedrock and overburden are assumed known, and computed using $\boldsymbol{S}_g$and $\boldsymbol{\varphi}$ in the target zone, with rock physics models. Note that $S_{w,i} = 1 - S_{g,i}$ and we will use this relationship repeatedly to remove $S_{w,i}$ as an unknown to be estimated. We define a matrix **AVA**=$\{AVA_{ij}\}$ to represent the seismic AVA data (observations), where $i = 1,2 \ldots n_t$ and $j = 1,2 \ldots n_a$. n_t and n_a are the numbers of time samples and incident angles respectively. The AVA observations and model predictions are related as follows

$$AVA_{ij} = M_{ij}^{AVA}(\boldsymbol{S_g}, \boldsymbol{\varphi}) + \varepsilon_{ij}^{s} \tag{6}$$

where M_{ij}^{AVA} is the *ij*th component of the model and ε_{ij}^{s} is corresponding measurement error.

We model the electromagnetic (Miotti and Giraud, 2015) observations in a similar manner. The second model, $\boldsymbol{M}^{EM}$, uses electrical conductivity σ in the overburden, target zone and bedrock to compute EM phase angles and amplitudes. The conductivity is assumed known in the overburden and bedrock and computed from $\boldsymbol{S}_g$and $\boldsymbol{\varphi}$ in the target zone using Archie's law. We use $S_{w,i} = 1 - S_{g,i}$ to obtain the water saturation values required by Archie's law. We define the matrix $\mathbf{EM} = \{EM_{ij}\}$ to represent the CSEM data matrix, with $i = 1,2 \ldots . n_o$ indexing receivers' offsets and $j = 1,2 \ldots n_f$ indexing CSEM frequencies. Since the amplitudes of the recorded electrical field span several orders of magnitude, we added a relative ratio ε_{ij}^{r} to the measurement error to adjust

its magnitude in the model. The relative ratio $\varepsilon_{ij}^{\mathrm{r}}$ is the normalization of each receiver offset to the furthest one.

$$EM_{ij} = M_{ij}^{EM}(\boldsymbol{S_g}, \boldsymbol{\varphi}) + \varepsilon_{ij}^{EM}\,\varepsilon_{\mathrm{ij}}^{\mathrm{r}} \tag{7}$$

Thus, for any given $(\boldsymbol{S_g}, \boldsymbol{\varphi})$, the likelihood of observing **AVA** and **EM** are given by

$$\mathrm{f}^{(AVA)}(\mathbf{AVA}|\mathbf{S_g}, \boldsymbol{\varphi}) \propto \exp[-\frac{1}{\mathrm{N_{AVA}}}\sum_{\mathrm{i=1}}^{\mathrm{n_t}}\sum_{\mathrm{j=1}}^{\mathrm{n_a}}\mathrm{w}^{\mathrm{AVA}}(\frac{\varepsilon_{\mathrm{ij}}^{\mathrm{AVA}}}{\sqrt{2}\sigma})^2] \tag{8}$$

$$\mathrm{f}^{(EM)}(\mathbf{EM}|\mathbf{S_g}, \boldsymbol{\varphi}) \tag{9}$$

$$\propto \exp\left[-\frac{1}{\mathrm{N_{AMP}}}\sum_{\mathrm{i=1}}^{\mathrm{n_o}}\sum_{\mathrm{j=1}}^{\mathrm{n_f}}\mathrm{w}^{\mathrm{EM}}(\frac{\varepsilon_{\mathrm{ij}}^{\mathrm{EM}}\varepsilon_{\mathrm{ij}}^{\mathrm{r}}}{\sqrt{2}\sigma})^2 - \frac{1}{\mathrm{N_{ANG}}}\sum_{\mathrm{i=1}}^{\mathrm{n_o}}\sum_{\mathrm{j=1}}^{\mathrm{n_f}}\mathrm{w}^{\mathrm{EM}}(\frac{\varepsilon_{\mathrm{ij}}^{\mathrm{EM}}\varepsilon_{\mathrm{ij}}^{\mathrm{r}}}{\sqrt{2}\sigma})^2\right]$$

where $\mathrm{w}^{\mathrm{AVA}}$ is the weight of seismic AVA incident angles, and w^{EM} is the weight of CSEM data which contains both EM amplitudes and phase angles. $\mathrm{w}^{\mathrm{AVA}}$ and w^{EM} are used to reduce the impact of small observational values. During joint inversion using both seismic and CSEM data, the weights $\mathrm{w}^{\mathrm{AVA}}$ and w^{EM} are set to be 0.2 and 1.2, respectively, in order to balance the contributions of seismic (with 80*5 data points) and CSEM (with 21*3 combinations of frequency and receiver locations) data to the likelihood functions. $\mathrm{N_{AVA}}$, $\mathrm{N_{AMP}}$ and $\mathrm{N_{ANG}}$ are the numbers of observations (seismic AVA, EM amplitude and phase angle) respectively.

Given these likelihoods, we use Bayes' formula to construct an expression for the posterior density $f(\boldsymbol{S_g}, \boldsymbol{\varphi} \mid \mathbf{AVA}, \mathbf{EM})$ as

$$f(\boldsymbol{S_g}, \boldsymbol{\varphi}|\mathbf{AVA}, \mathbf{EM}) \propto f^{(AVA)}(\mathbf{AVA}|\boldsymbol{S_g}, \boldsymbol{\varphi})\, f^{(EM)}(\mathbf{EM}|\boldsymbol{S_g}, \boldsymbol{\varphi})\, \pi(\boldsymbol{S_g})\, \pi(\boldsymbol{\varphi}). \tag{10}$$

here, $\pi(:)$ denotes our prior beliefs regarding $\boldsymbol{S_g}$ and $\boldsymbol{\varphi}$. We assume that they are independent and can be modeled as uniform distributions: $S_{g,i} \sim U(0,1)$ and $\varphi_i \sim U(0, 0.3)$. The posterior distribution is too complex to be derived analytically and consequently, we will approximate $f(\boldsymbol{S_g}, \boldsymbol{\varphi} \mid \mathbf{AVA}, \mathbf{EM})$ by drawing samples from it using MCMC and constructing kernel density estimates of the distribution from them.

2.3 Multi-Chain MCMC Framework

A multi-chain MCMC framework is used to generate posterior densities of model parameters, given observational data and a prior density on model parameters. A single-chain MCMC method describes a random walk through the parameter space $\theta = \{\boldsymbol{S_g}, \boldsymbol{\varphi}\}$. In our case, the steps in the random walk are generated using a Metropolis-Hastings (MH) sampler. It requires a proposal distribution (most commonly a multivariate normal distribution *q(μ, Γ)*, where μ and Γ are its mean and covariance matrix respectively. Assume that the MCMC method has taken *i* steps in its random walk, and its current position in the parameter space is θ_i. The MH sampler first samples a candidate Y from the proposal density function $q(Y|\theta_i, \Gamma)$. It runs the forward model and computes the right hand side of Eq. 5, which is equal to the posterior density $f(\mathbf{AVA}, \mathbf{EM}\,|Y)$ modulo a scaling constant. It then calculates the acceptance ratio as

$$\alpha(\theta_i, Y) = \min\left(1, \frac{f(\mathbf{AVA}, \mathbf{EM}|Y)\; q(Y|\theta_i, \Gamma)}{f(\mathbf{AVA}, \mathbf{EM}|\theta_i)\; q(\theta_i|Y, \Gamma)}\right) \tag{11}$$

If $\alpha(\theta_i, Y) > U$, then the new sample is $\theta_{i+1} = Y$, else the new sample is $\theta_{i+1} = \theta_i$. U is a random number drawn from a uniform $\mathcal{U}[0, 1]$ distribution. MCMC usually requires more than 10,000 evaluations of the forward simulation model, which can be very expensive. This cost is reduced in

two ways. First, we adapt (recomputed) Γ using existing samples so that *q(:, :)* resembles an inflated version of the posterior distribution; this adaptation is performed in the manner described by the DRAM algorithm (Haario et al., 2006) . Note that we do not use Delayed Rejection component of the DRAM method in our MCMC approach; strictly speaking, our sampler only performs Adaptive Metropolis (AM) sampling. Secondly, we amortize the sampling cost over multiple chains, as described in (Solonen et al., 2012) . While AM might periodically update its proposal covariance Γ one needs to start it with an initial proposal covariance. This presents a challenge – if it is too conservative (too narrow), the MCMC method will only explore in the neighborhood of the initial starting point and take a large number of steps to explore the parameter space fully. If Γ is too wide, most of the proposals will be far from the region with most of the probability mass, and the proposals will mostly be rejected, leading to chains that do not mix. In order to circumvent this problem, we start the sampling procedure using DREAM (Vrugt et al., 2009) , which does not require a proposal distribution. Once a number of samples, sufficient to produce a crude approximation of the posterior density, have been collected, we switch to a 4-chain AM sampler.

3 Results

3.1 Synthetic studies

As shown in Fig. 1, a realistic layered reservoir model (Chen et al., 2004) (Hou et al., 2006) is considered in our study. The synthetic reservoir model includes five layers with a thickness of 50 m and zero oil saturation. Thus Sw + Sg = 1 in any layer. The target horizon is 1050m below the seafloor that includes 500m of seawater and a 550 m thick overburden under the seawater. From the upper to the bottom layers, the true gas saturation values are 0.05, 0.95, 0.4, 0.9 and 0.1,

respectively. The corresponding true porosity values are 0.15, 0.25, 0.15, 0.1 and 0.05, respectively. Seismic AVA data used for this study are normal move out (NMO) corrected angle gathers generated by convolving a 50 Hz Ricker wavelet with the angle-dependent reflectivity for each layer interface. The data is sampled at 2ms resolution for five incident angles (0°, 10°, 20°, 30°, and 40°) and calculated using the Zoeppritz equation. The marine CSEM system consists of a ship-towed electric dipole source and a number of seafloor-deployed recording instruments capable of recording orthogonal electric fields. The electric dipole transmitter is 200m in length and 50m off the seafloor to avoid collision with stationary receiver systems. The CSEM data includes the amplitude and phase as recorded by 21 receivers at 0.5, 1, and 2 Hz, respectively. The receivers' offsets are set up to 5000m. The prior distributions of porosity and gas saturation at each layer are assumed to be uniform within [0, 0.3] and [0, 1], respectively.

3.2 Seismic-Only Inversion

A seismic-only inversion is first performed using four MCMC chains. The chains are run for 10,000 generations i.e., each chain runs for 10,000 steps, and a total of 40,000 samples are collected. The covariance matrix is updated every 20 steps. The posterior bounds (2.5^{th} and 97.5^{th} percentiles) for porosity are listed in Table 2, and they are quite tight. This is not surprising since the AVA data is quite sensitive to porosity.

Adjusting the bounds to the narrower ones in Table 2 can significantly increase the convergence when inverting for all 10 variables i.e., porosity and gas saturation in the 5 layers of the target zone. Therefore, these updated bounds for porosity are later used for joint inversion using both seismic and CSEM data.

The marginalized posterior PDFs of gas saturation and porosity using seismic-only inversion are shown in Fig. 2. The PDFs indicate accurate estimation of porosity with relatively low uncertainty (i.e., narrow bounds) in each layer. For gas saturation estimation, seismic-only inversion infers the upper layers (e.g., layer 1) accurately, with relatively small uncertainty. The predicted modes of the PDFs are close to the actual values for the rest of the layers, but the uncertainty level of layer 3, 4 and 5 are large. This is expected because seismic AVA responses are less sensitive to gas saturation changes.

Next, we evaluate the effect of noise levels in the observations on reservoir parameter estimation. We generated identical and independently distributed standard normal ($\mathcal{N}(\mu = 0,\ \sigma^2 = 1)$) random deviates and added them to the observations. In order to investigate the effect of a steadily worsening signal-to-noise ratio, the random deviates were multiplied by a factor. In the tests below, we varied the magnitude of the factor from 10% to 30% of the standard deviation of observations at each of the receivers/sensors. The marginalized posterior PDFs of porosity using observations with various levels of noise are shown in Fig. 3. The porosity estimation is acceptable when the noise level is less than 25%; further, the uncertainty levels are comparable. When the noise level exceeds 25%, the multi-chain MCMC does not converge to the true parameter value and the chains cannot mix well.

3.3 Joint Inversion

This section demonstrates the benefits adding CSEM data to AVA data when estimating $\boldsymbol{S_g}$, and indirectly $\boldsymbol{S_w}$. Although Archie's law states that CSEM data can be sensitive to reservoir water/gas

saturations, such sensitivity should vary with offset distance and operating frequency. Therefore, a sensitivity analysis was performed to discover the most sensitive ranges and frequencies in the CSEM data given our model setup. Quasi Monte Carlo (QMC) sampling is an efficient sampling technique to explore the multi-dimensional parameter space and has been widely used in the sensitivity analysis (Niederreiter, 1978),(Hou et al., 2012),(Ren et al., 2016). 2000 QMC sample sets were generated for water saturation (alternatively, gas saturation) for the 5 layers, and the resulting ensemble of CSEM responses (amplitude and phases) are shown as boxplots at each location in Fig. 4. The CSEM signals seem to be the most sensitive to reservoir saturation when the receiver is located between distances of 500m to 5,000m. Furthermore, since the amplitude of the CSEM data decreases rapidly with the increasing offsets, receivers deployed at near offsets receive more stable and informative signals. This is similar to seismic AVA data, where signals with smaller incidence angle data are stronger.

Comparing the seismic inversion and joint inversion results, we find insignificant differences in the porosity estimates, but the improvement in gas saturation estimation is significant, especially for the bottom layers. In addition, the joint inversion greatly reduces the uncertainty in gas saturation estimates, as can be seen for layers 2, 4, and 5 in Fig. 5. The joint inversion clearly identified the two high-gas concentration layers (layer 2 and 4).

We also investigated the impact of observational noise on the gas saturation estimation, with noise levels of 10, 15, 20, 25, and 30 percent, in both the amplitude and phase components. The corresponding PDFs of gas saturation are shown in Fig. 6. The marginalized posterior PDFs are

reliable with noise levels up to 15%. Although gas saturation seems to have been estimated accurately in the top and bottom layers when the noise level is high (e.g., 30%), the corresponding uncertainty can be very high. Moreover, the inversion accuracy might not increase monotonically with the noise level because it is also affected by the way noises were generated and added.

3.4 Validation

Comparing the modes or *maximum a posteriori* estimates of PDFs to the true values of gas saturation and porosity is one of the ways of checking for the accuracy of an inversion. Being able to reproduce the observed AVA and EM data provides a second and independent validation of the inversion results. We draw 1,000 samples of $(\boldsymbol{S_g}, \boldsymbol{\varphi})$ from the posterior distribution with no noise, 10% noised and 30% noise and proceed to perform forward simulations with them. The predictions of this ensemble of runs are summarized in Fig. 7 and 8, for the seismic and CSEM observations respectively. For the cases of no noise and 10% noise, the dotted line (median of the 1000 predictions) is close to the observations for seismic data (Fig. 7), and the amplitudes and phase in CSEM data (Fig. 8). The inter-quartile range brackets most of the observations, note that the horizontal axis in Fig. 8 is log-transformed and the amplitudes with disagreement between predictions and observations are at offsets where the amplitudes are two orders of magnitude smaller than the near offsets. And the degree of agreement of the CSEM amplitude to observational data is about the same as that of the phase angle. When the noise level increases to 30%, most of the observations are outside of the inter-quartile predictions range, especially for the amplitudes and phases in CSEM data. The conclusions are consistent with our posterior PDFs. Finally, we summarize the goodness-of-fit between the observations and ensemble of predictions using the Continuous Rank Probability Score (CRPS), Mean Absolute Error (MAE) and the optimal

fingerprint distance d_{OF}. The first two metrics have dimensions of the variable being quantified while the latter is non-dimensional. Below we provide a summary of the metrics; details can be found in (Thorarinsdottir et al., 2013) and (Gneiting and Raftery, 2007)

Let $y_i^{(obs)}$be an observation e.g., it could be one of the dots in Fig. 7. Corresponding to $y_i^{(obs)}$ are the N = 1,000 predictions $y_{i,j}, j = 1 \cdots N$. In such a case, one can construct $F_i(y)$, the cumulative distribution function (CDF) for $y_{i,j}$. The Heaviside function $H\left(y - y_i^{(obs)}\right)$ is the CDF of the observation $y_i^{(obs)}$. The CRPS for any observation $y_i^{(obs)}$is given by

$$crps\left(y_i^{(obs)}\right) = \int_{-\infty}^{\infty} \left(F_i(y) - H\left(y - y_i^{(obs)}\right)\right)^2 dy \tag{12}$$

The CRPS for all the observations is simply a mean of the CRPSs' of the individual ones. Similarly, we define the MAE for a given observation

$$mae\left(y_i^{(obs)}\right) = \sum_{j=1}^{N} \left|y_i^{(obs)} - y_{i,j}\right|. \tag{13}$$

Finally, let $\boldsymbol{y}^{(obs)} = \left\{y_i^{(obs)}\right\}$ and $\overline{\boldsymbol{y}}$ be the mean prediction of the ensemble of 1,000 runs. We model the N predictions as draws from a multivariate Gaussian distribution $N(\overline{\boldsymbol{y}}, \gamma)$, where the exact form of the covariance matrix γ is left to the modeler. We model γ as a diagonal matrix. The optimal finger print distance $d_{OF}$is defined as

$$d_{OF} = \left(\boldsymbol{y}^{(obs)} - \overline{\boldsymbol{y}}\right)^T \gamma^{-1} \left(\boldsymbol{y}^{(obs)} - \overline{\boldsymbol{y}}\right) \tag{14}$$

In Table 3 we summarize the comparison between AVA observations and 1,000 ensemble predictions of the same, as plotted in Fig. 7. We see clearly that predictions at Receiver 1 (0^o) are the best, resulting in the smallest values for all 3 metrics. In Table 4, we tabulate the same metrics for the CSEM phase observations and predictions, as plotted in Fig. 8 (top). We see that the 0.5 Hz measurement channel shows best agreement between observations and predictions, as captured by the dimensional metrics (CRPS and MAE) as well as the non-dimensional d_{OF}. In Table 5, we summarize the agreement between CSEM amplitude observations and posterior predictions as plotted in Fig. 8 (bottom). The 1 Hz channel has the smallest dimensional metrics, primarily due to the smaller measured amplitudes; the non-dimensional metric, which is insensitive to the magnitude of the measurements, shows that the 0.5 Hz channel's observations are reproduced best by the ensemble predictions. This is likely because the absolute magnitudes of the lower frequency signals are larger, and the misfits between simulated and observed magnitudes are relatively bigger and therefore dominates the higher frequency ones in the likelihood functions.

3.5 Multi-Chain MCMC Inversion

The inversion results with different numbers of chains are compared in Fig. 9. The posterior PDFs are plotted using the same number of sample sets, i.e., 40,000 iterations for the single chain, 10,000 iterations for the 4-chain inversion, and 2,500 iterations for the 16-chain inversion, and so on. Figure 9 shows that the PDFs are comparable, prove that multi-chain MCMC can achieve convergence earlier (in terms of wall-clock time) than the single-chain version, and the scalability is almost linear.

The scalability of the multi-chain MCMC method, as the number of chains is increased, is difficult to assess empirically. This is due to two reasons. First, the number of steps required to reach a converged PDF depends partially on the starting points of the chains, which change as we vary the number of chains. The second difficulty arises from the fact that the ratio of communication to computational costs depend immensely on the forward problem.

Consider an inversion with P chains, solving for M parameters. The chains sample independently for q steps, after which they update their proposal covariance. This requires an all-to-all communication between all processors, with each processor exchanging qM numbers. This broadcast, theoretically, can be accomplished in $P \log_2 P$ steps, incurring a total communication cost of $K_1\ q\ M\ P\ \log_2\ P$. Since both q and M for most inverse problems will be small, the communication costs do not scale badly. On the other the computational cost of the forward problem, in our inversion, scales as $K_2\ q\ M$. Therefore, the ratio of communication to computation cost scales as $K_1\ P \log_2 P / K_2$. Depending upon the values assumed by K_1 and K_2, the ratio can be quite small and the inverse problem will scale reasonably well in practice. In our case, each invocation of the forward model takes 0.41 seconds while the communication costs of doing a broadcast of 20 x 10 = 200 numbers, over 4 processors is minuscule and difficult to measure.

4 Conclusion

In this study, we propose a multi-chain MCMC-Bayesian framework to estimate marine reservoir gas saturation and porosity using seismic AVA and marine CSEM data. We demonstrate the ability of our approach to solve nonlinear statistical inverse problems by constructing a 10-dimensional posterior density for gas saturations and porosities of a layered underwater gas reservoir. The

posterior density is complex and is approximated by samples drawn by a multi-chain MCMC technique that is a hybrid of DREAM and AM samplers. The probability density functions of gas saturations and porosities capture the true values and provide a measure of the uncertainty in the estimated quantities. We also find that multi-chain inversion converges to the final posterior density faster than the single-chain, and the scalability is almost linear.

For a layered synthetic model, our approach can identify and confirm the locations of gas-rich layers regardless of whether they are shallow or deep. Seismic-only inversion can identify the porosity correctly but has difficulties when estimating gas saturations. With the information provided by seismic-only inversion in hand, incorporation of CSEM data decreases the uncertainty in gas saturation estimates and increases the ability to distinguish high or low gas concentrations in deep layers.

The investigation of the impact of observational noise shows that our approach can capture the true values of porosity using data with a noise level of up to 25% in the observed seismic AVA data. It can correctly estimate gas saturation with up to 15% noise in CSEM data. Beyond these noise levels, the multi-chain MCMC has difficulty in mixing and the sampler does not converge to a distribution. We also find that the very top and bottom layers are better characterized in the current setup.

Acknowledgments

This work is supported by the Office of Science Advanced Scientific Computing Research (ASCR). Pacific Northwest National Laboratory is operated for the DOE by Battelle Memorial

Institute under Contract DE-AC05-76RLO1830. Sandia National Laboratories is a multimission laboratory managed and operated by National Technology and Engineering Solutions of Sandia LLC, a wholly owned subsidiary of Honeywell International Inc. for the U.S. Department of Energy's National Nuclear Security Administration under contract DE-NA0003525.

References

Aki, K., and Richards, P., 1980, Quantative seismology: Theory and methods: Freeman and Company, v. 2.

Archie, G. E., 1942, The electrical resistivity log as an aid in determining some reservoir characteristics: Transactions of the AIME, v. 146, no. 01, p. 54-62.

Castagna, J. P., and Backus, M., 1993, AVO analysis-tutorial and review: Offset-dependent reflectivity: theory and practice of AVO analysis, p. 3-36.

Chen, J., Hoversten, G. M., Vasco, D., Rubin, Y., and Hou, Z., Joint inversion of seismic AVO and EM data for gas saturation estimation using a sampling-based stochastic model, *in* Proceedings 2004 SEG Annual Meeting2004.

Chen, J., Hoversten, G. M., Vasco, D., Rubin, Y., and Hou, Z., 2007, A Bayesian model for gas saturation estimation using marine seismic AVA and CSEM data: Geophysics, v. 72, no. 2, p. WA85-WA95.

D e¸ bski, W., and Tarantola, A., 1995, Information on elastic parameters obtained from the amplitudes of reflected waves: Geophysics, v. 60, no. 5, p. 1426-1436.

Du, Z., and MacGregor, L. M., Reservoir characterization from joint inversion of marine CSEM and seismic AVA data using Genetic Algorithms: a case study based on the Luva gas field, *in* Proceedings 2010 SEG Annual Meeting2010, Society of Exploration Geophysicists.

Dvorkin, J., and Nur, A., 1996, Elasticity of high-porosity sandstones: Theory for two North Sea data sets: Geophysics, v. 61, no. 5, p. 1363-1370.

Fliedner, M., Treitel, S., Frenkel, M., and MacGregor, L., 2011, Fast stochastic inversion of marine CSEM and seismic data with the Neighbourhood Algorithm: 81th Ann. Inter-nat. Mtg. Soc. Expl. Geophys., Expanded Abstracts, v. 30, p. 2517-2522.

Gassmann, F., 1951, Elastic waves through a packing of spheres: Geophysics, v. 16, no. 4, p. 673-685.

Gneiting, T., and Raftery, A. E., 2007, Strictly proper scoring rules, prediction, and estimation: Journal of the American Statistical Association, v. 102, no. 477, p. 359-378.

Haario, H., Laine, M., Mira, A., and Saksman, E., 2006, DRAM: efficient adaptive MCMC: Statistics and computing, v. 16, no. 4, p. 339-354.

Hou, Z., Huang, M., Leung, L. R., Lin, G., and Ricciuto, D. M., 2012, Sensitivity of surface flux simulations to hydrologic parameters based on an uncertainty quantification framework applied to the Community Land Model: Journal of Geophysical Research: Atmospheres, v. 117, no. D15.

Hou, Z., Rubin, Y., Hoversten, G. M., Vasco, D., and Chen, J., 2006, Reservoir-parameter identification using minimum relative entropy-based Bayesian inversion of seismic AVA and marine CSEM data: Geophysics, v. 71, no. 6, p. O77-O88.

Hoversten, G. M., Gritto, R., Washbourne, J., and Daley, T., 2003, Pressure and fluid saturation prediction in a multicomponent reservoir using combined seismic and electromagnetic imaging: Geophysics, v. 68, no. 5, p. 1580-1591.

Lang, X., and Grana, D., Bayesian Rock Physics Inversion of Acoustic and Electrical Properties for Rock-Fluid Property Estimation, *in* Proceedings 2015 SEG Annual Meeting2015, Society of Exploration Geophysicists.

Liang, F., Liu, C., and Carroll, R., 2011, Advanced Markov chain Monte Carlo methods: learning from past samples, John Wiley & Sons.

Miotti, F. M., and Giraud, J., 2015, Joint inversion of attributes, Google Patents.

Niederreiter, H., 1978, Quasi-Monte Carlo methods and pseudo-random numbers: Bulletin of the American Mathematical Society, v. 84, no. 6, p. 957-1041.

Plessix, R. E., and Bork, J., 2000, Quantitative estimate of VTI parameters from AVA responses: Geophysical Prospecting, v. 48, no. 1, p. 87-108.

Ren, H., Hou, Z., Huang, M., Bao, J., Sun, Y., Tesfa, T., and Leung, L. R., 2016, Classification of hydrological parameter sensitivity and evaluation of parameter transferability across 431 US MOPEX basins: Journal of Hydrology, v. 536, p. 92-108.

Shuey, R., 1985, A simplification of the Zoeppritz equations: Geophysics, v. 50, no. 4, p. 609-614.

Solonen, A., Ollinaho, P., Laine, M., Haario, H., Tamminen, J., and Järvinen, H., 2012, Efficient MCMC for climate model parameter estimation: parallel adaptive chains and early rejection: Bayesian Analysis, v. 7, no. 3, p. 715-736.

Thorarinsdottir, T. L., Gneiting, T., and Gissibl, N., 2013, Using proper divergence functions to evaluate climate models: SIAM/ASA Journal on Uncertainty Quantification, v. 1, no. 1, p. 522-534.

Vrugt, J. A., Ter Braak, C., Diks, C., Robinson, B. A., Hyman, J. M., and Higdon, D., 2009, Accelerating Markov chain Monte Carlo simulation by differential evolution with self-adaptive randomized subspace sampling: International Journal of Nonlinear Sciences and Numerical Simulation, v. 10, no. 3, p. 273-290.

Ward, S. H., and Hohmann, G. W., 1988, Electromagnetic theory for geophysical applications: Electromagnetic methods in applied geophysics, v. 1, no. 3, p. 131-311.

Figure

Figure 1. Schematic map of the inversion domain. The target zone is parameterized by S_w, S_g and φ. The reservoir is located below a 550-thick overburden and a 500m-thick seawater layer. Seismic velocity, density, bulk moduli, and electrical conductivity above and below the reservoir are assumed to be known.

Figure 2. Seismic-only inversion for estimating gas saturation and porosity. The left panels are the estimates of gas saturation from top to bottom layers; the right panels are the porosities of the same layers. The red vertical lines are the true values for each variable.

Figure 3. Porosity estimates from seismic-only inversion using data with different levels of Gaussian noise.

Figure 4. Boxplot for the sensitivity study of receivers' range for CSEM model

Figure 5. Marginalized posterior PDFs of gas saturation and porosity from joint seismic and CSEM inversion. The solid black lines are PDFs from the seismic-only inversion and the dashed green lines are from the joint inversion. The vertical red lines are the true values for each variable.

Figure 6. Gas saturation estimation using joint seismic and CSEM inversion with added Gaussian noise. The vertical red lines are the true values for each variable.

Figure 7. Posterior predictive simulations of seismic AVA responses using 1,000 samples of gas saturation and porosity drawn from the posterior density with (a) no noise, (b) 10% noise added and (c) 30% noise added. The symbols are the observations and the dotted line the median prediction. The error bars denote the inter-quartile range and the dashed lines are the outliers. Each subplot corresponds to one receiver.

Figure 8. Posterior predictive simulations of CSEM amplitude and phase angle responses for (a) no noise, (b) 10% noise added and (c) 30% noise added. The symbols are the observations and the dotted line the median prediction. The error bars denote the inter-quartile range and the dashed lines are the outliers. Each subplot corresponds to one frequency.

Figure 9. Posterior PDFs of gas saturations from the joint inversion with different numbers of chains.

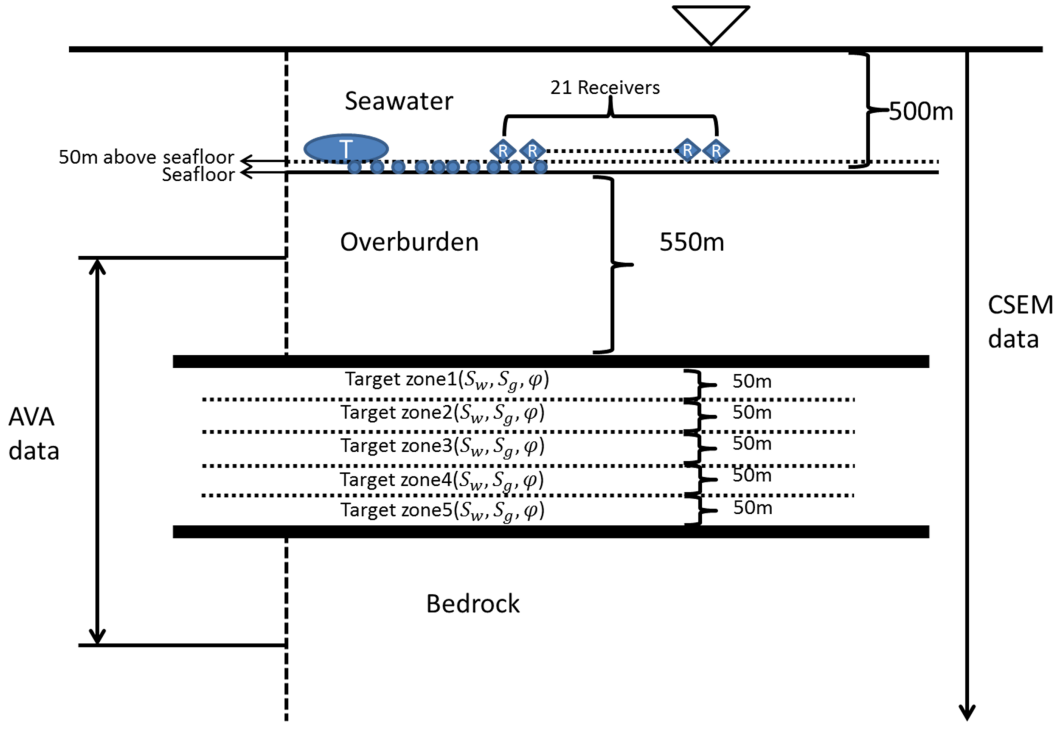

Figure 1.

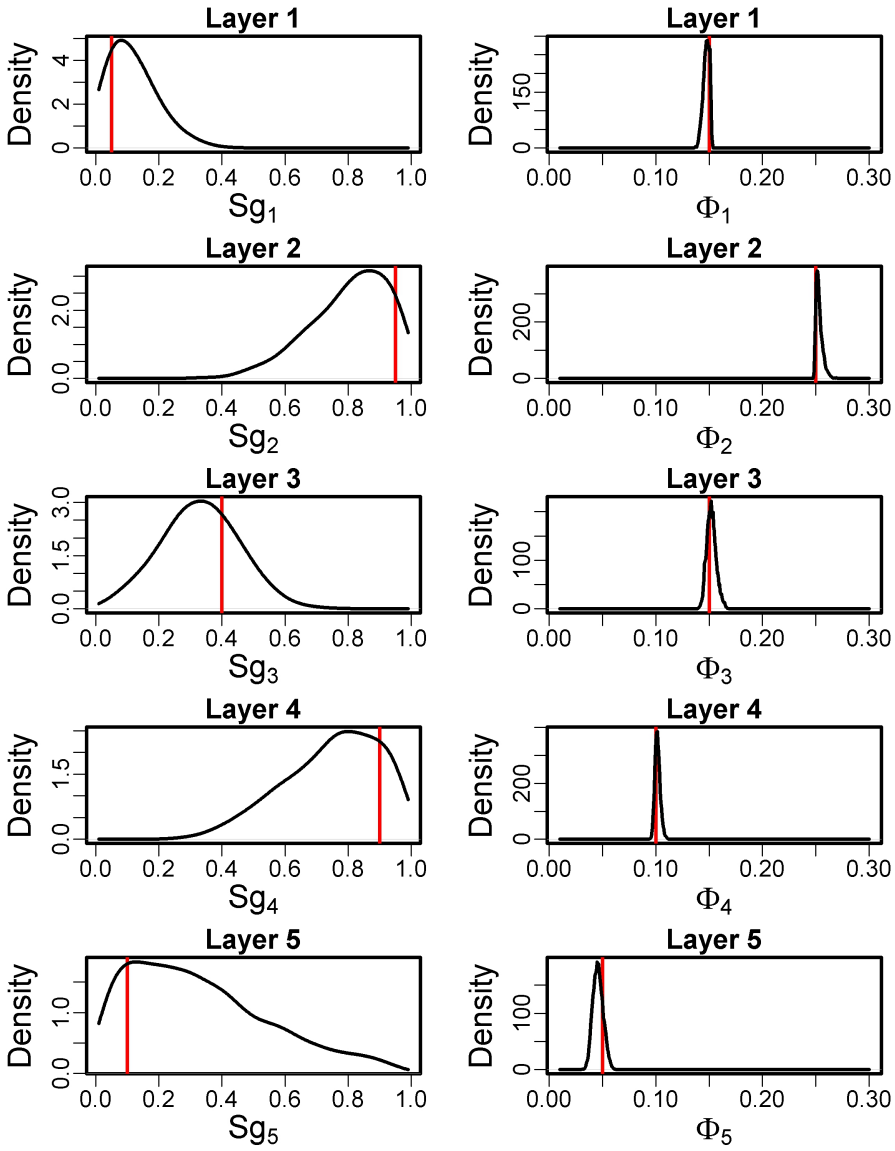
Layer 1
Density
Sg1
Φ1
Layer 2
Sg2
Φ2
Layer 3
Sg3
Φ3
Layer 4
Sg4
Φ4
Layer 5
Sg5
Φ5

Figure 2.

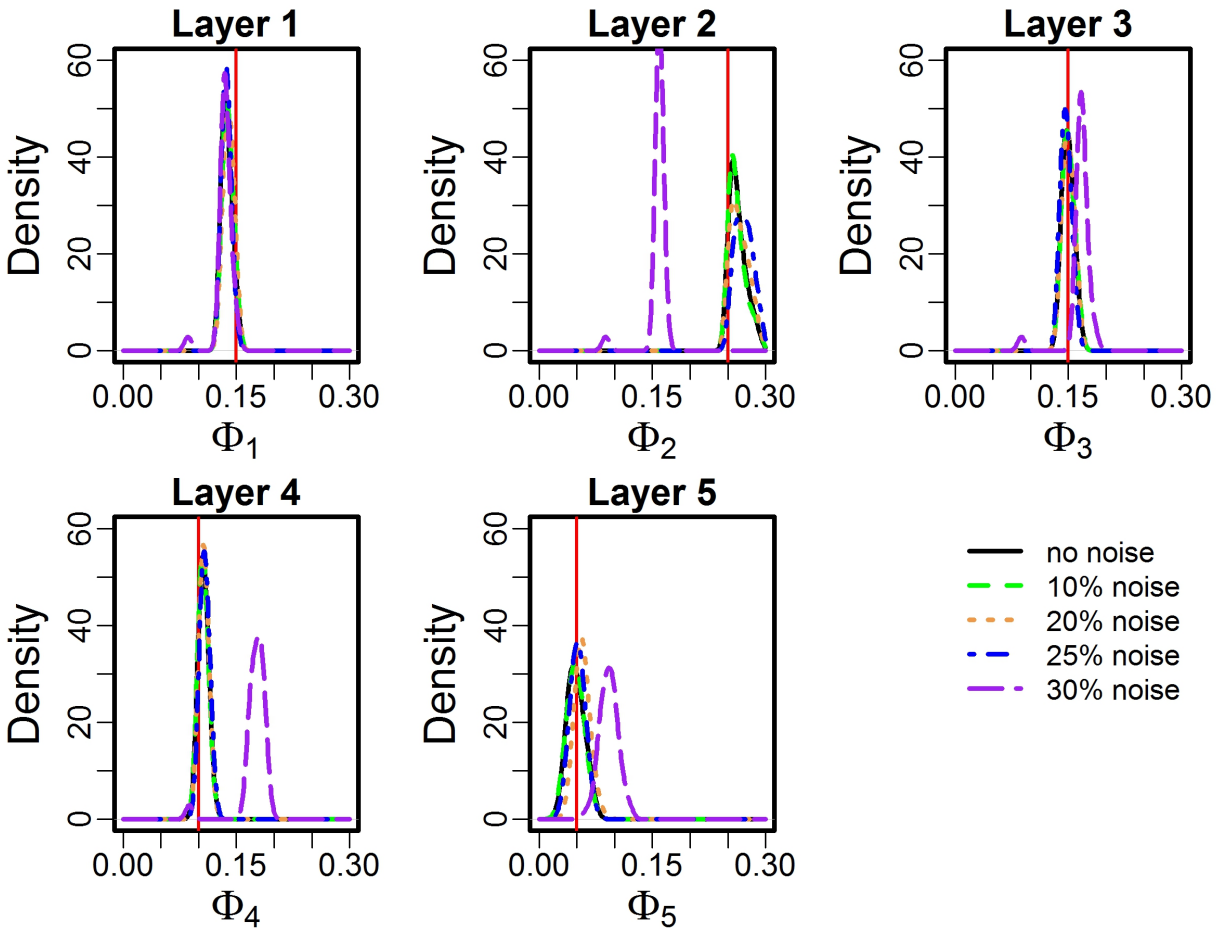
Layer 1
Layer 2
Layer 3
Layer 4
Layer 5
Density
0
20
40
60
0.00
0.15
0.30
Φ_1
Φ_2
Φ_3
Φ_4
Φ_5
no noise
10% noise
20% noise
25% noise
30% noise

Figure 3.

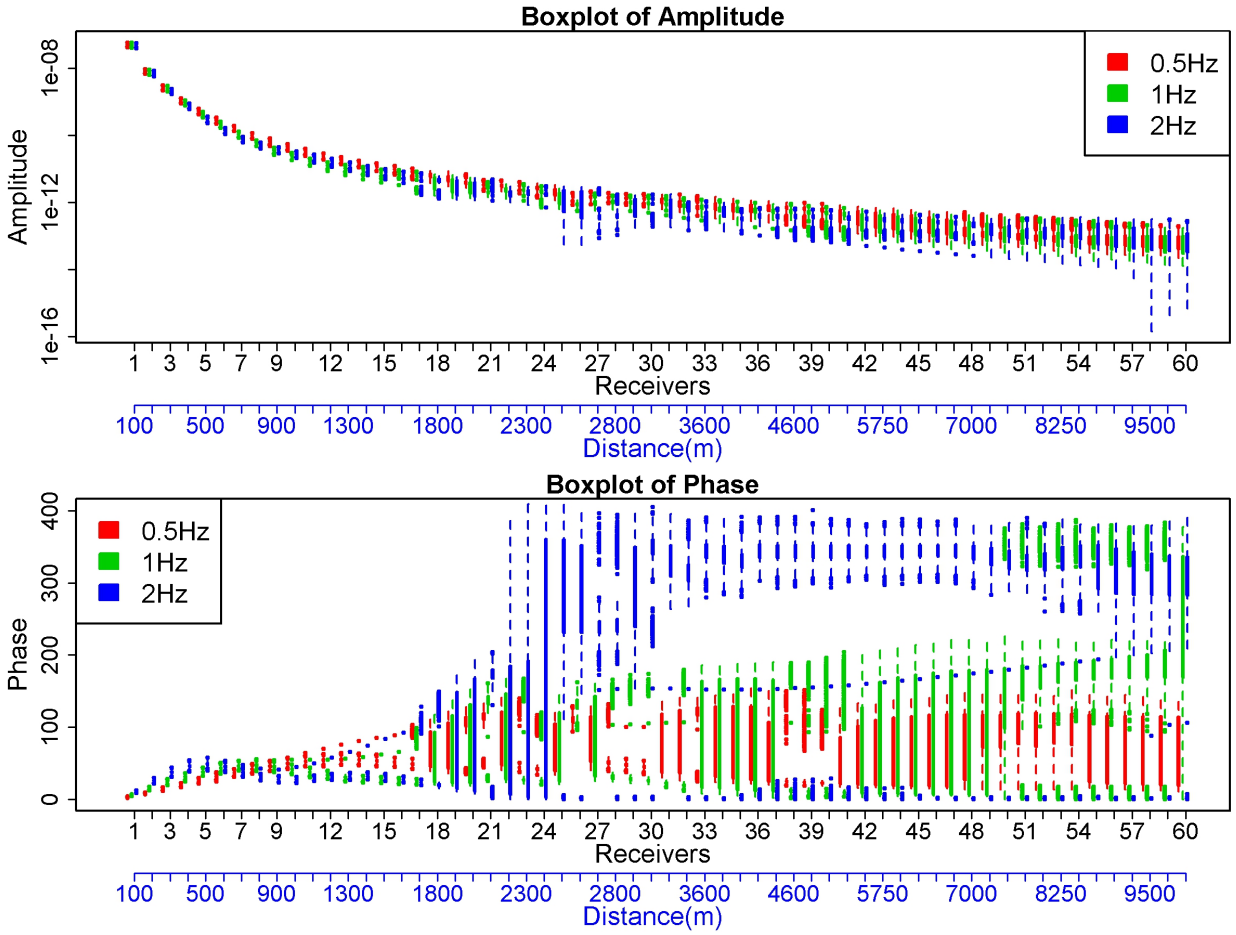
Boxplot of Amplitude
Amplitude
1e-08
1e-12
1e-16
0.5Hz
1Hz
2Hz
1 3 5 7 9 12 15 18 21 24 27 30 33 36 39 42 45 48 51 54 57 60
Receivers
100 500 900 1300 1800 2300 2800 3600 4600 5750 7000 8250 9500
Distance(m)
Boxplot of Phase
Phase
0 100 200 300 400
0.5Hz
1Hz
2Hz
1 3 5 7 9 12 15 18 21 24 27 30 33 36 39 42 45 48 51 54 57 60
Receivers
100 500 900 1300 1800 2300 2800 3600 4600 5750 7000 8250 9500
Distance(m)

Figure 4.

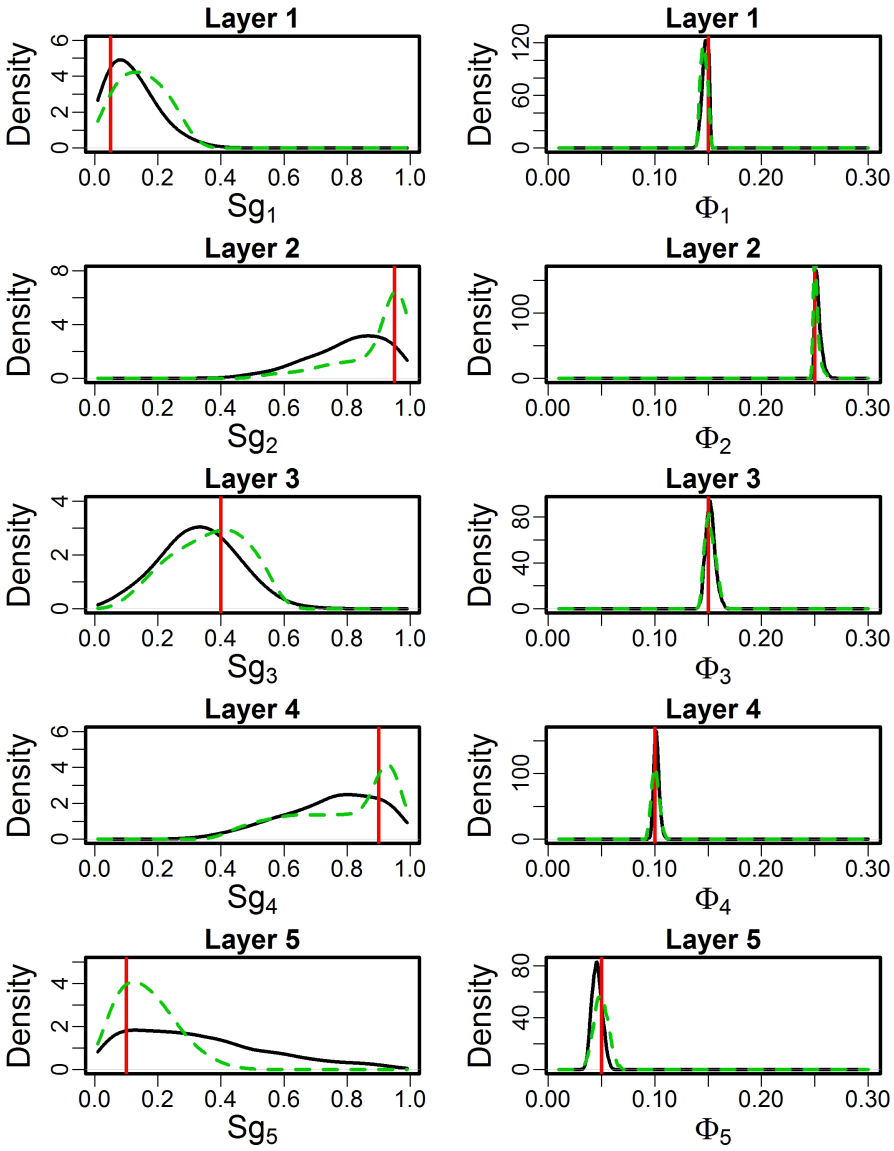
Layer 1
Density
Sg1
Φ1
Layer 2
Sg2
Φ2
Layer 3
Sg3
Φ3
Layer 4
Sg4
Φ4
Layer 5
Sg5
Φ5

Figure 5.

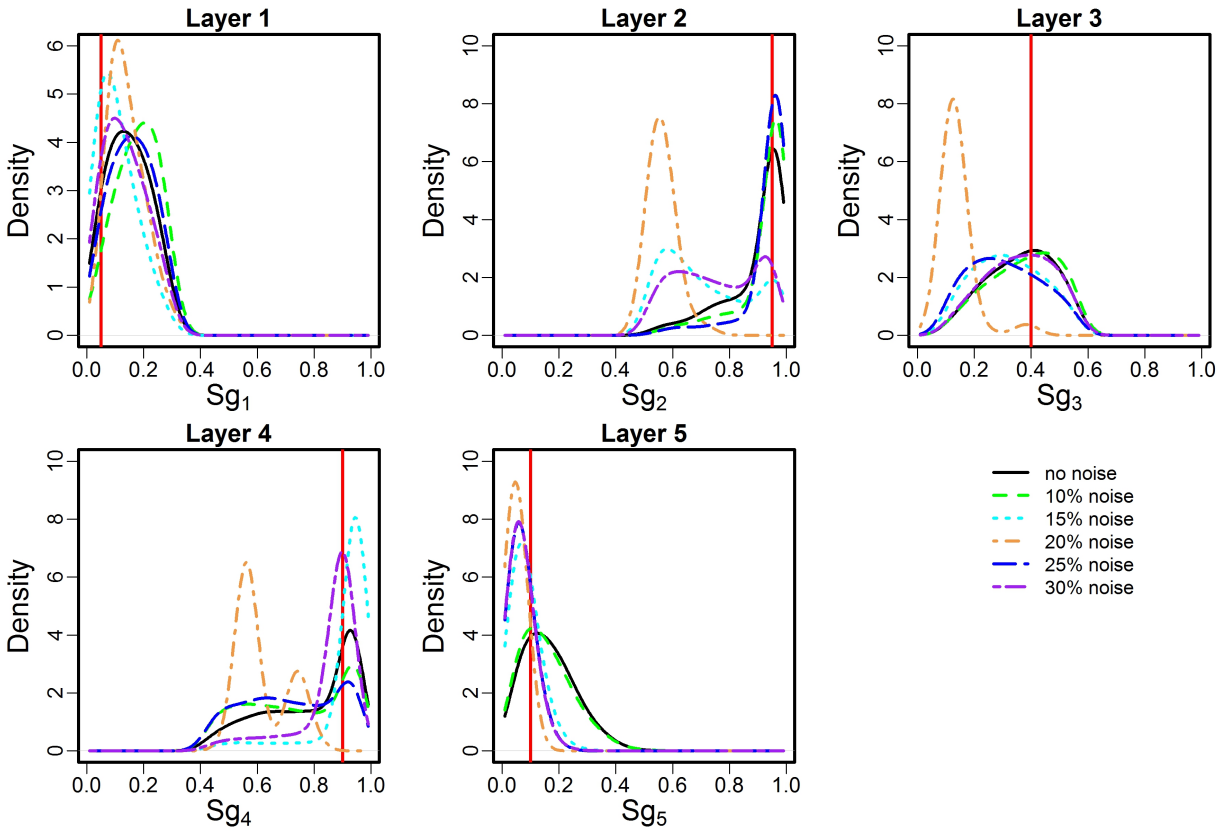
Layer 1
Layer 2
Layer 3
Layer 4
Layer 5
Density
Sg1
Sg2
Sg3
Sg4
Sg5
no noise
10% noise
15% noise
20% noise
25% noise
30% noise

Figure 6.

(a)

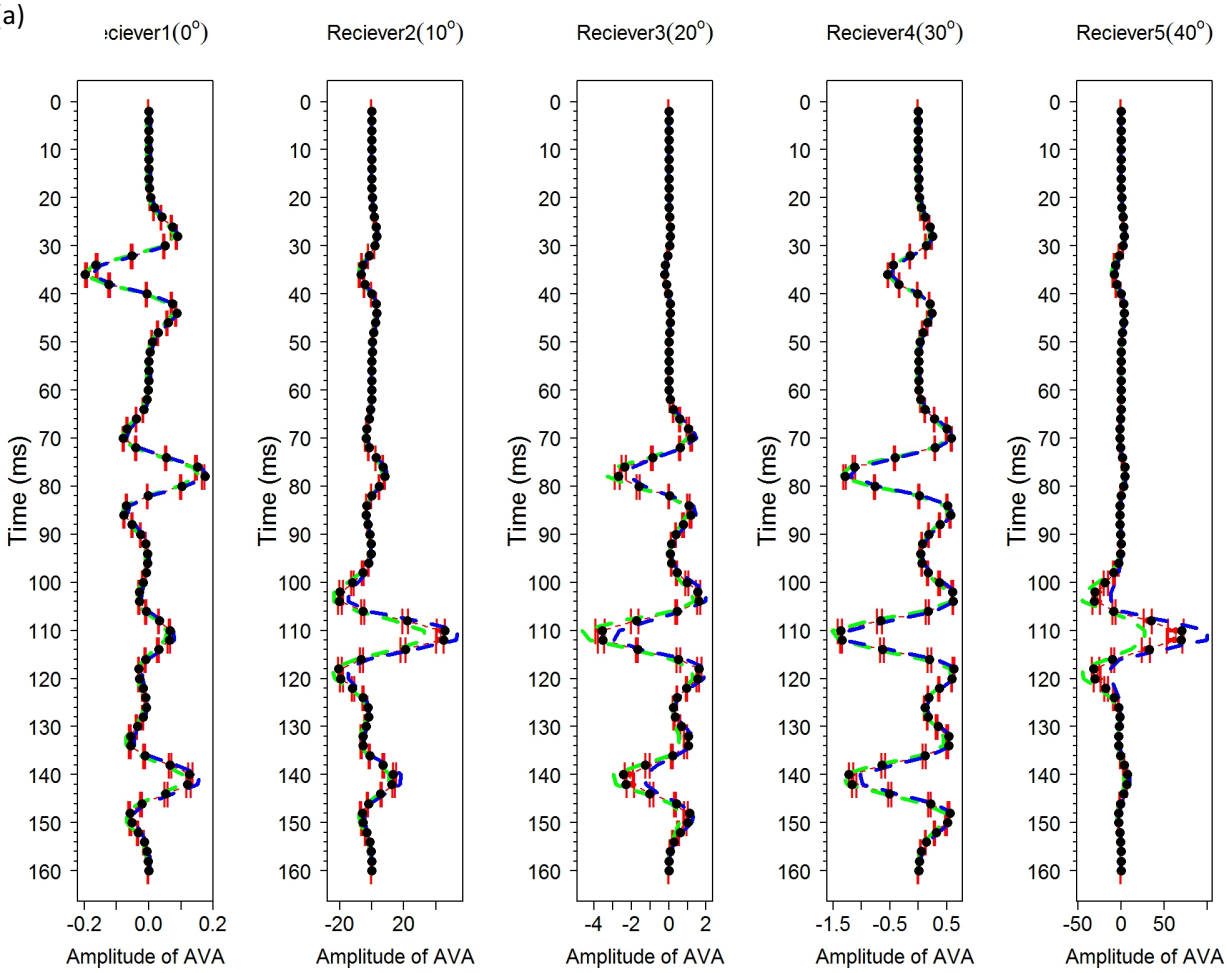
ciever1(0°)
Reciever2(10°)
Reciever3(20°)
Reciever4(30°)
Reciever5(40°)
Time (ms)
Amplitude of AVA

(b)

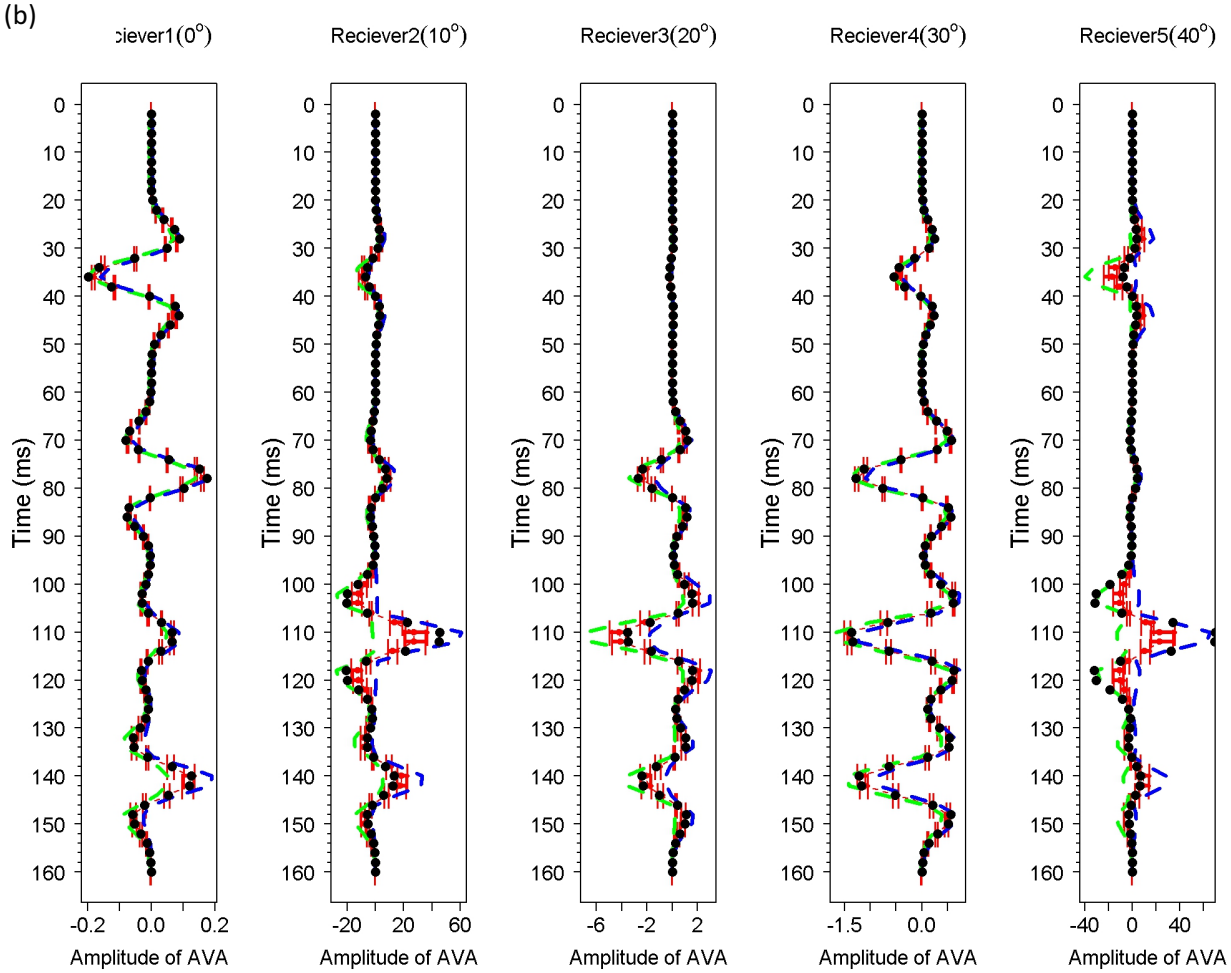
ciever1(0°)
Reciever2(10°)
Reciever3(20°)
Reciever4(30°)
Reciever5(40°)
Time (ms)
Amplitude of AVA
-0.2 0.0 0.2
-20 20 60
-6 -2 2
-1.5 0.0
-40 0 40

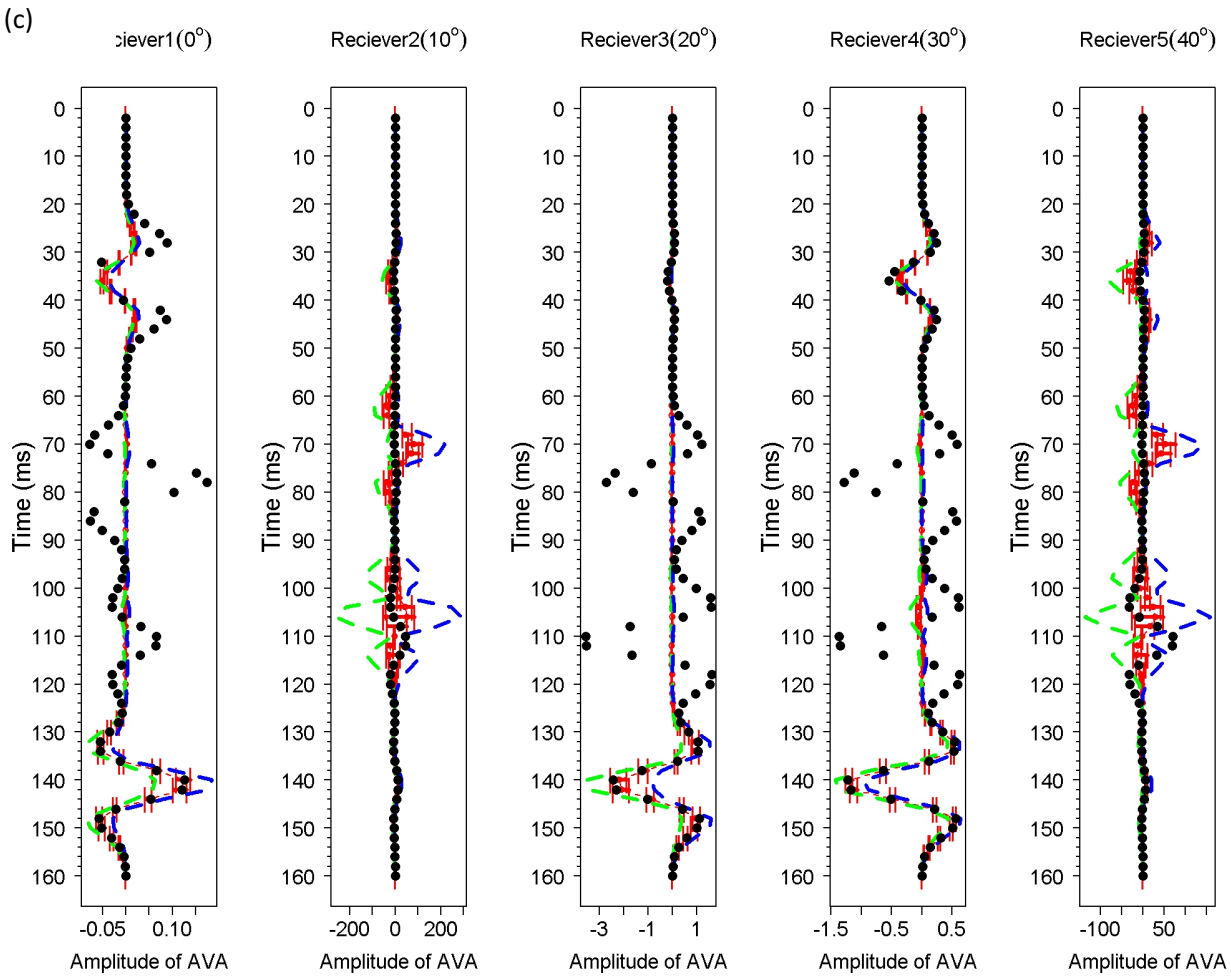
(c)
ciever1(0°)
Reciever2(10°)
Reciever3(20°)
Reciever4(30°)
Reciever5(40°)
Time (ms)
Amplitude of AVA
-0.05
0.10
-200
0
200
-3
-1
1
-1.5
-0.5
0.5
-100
50

Figure 7.

(a)

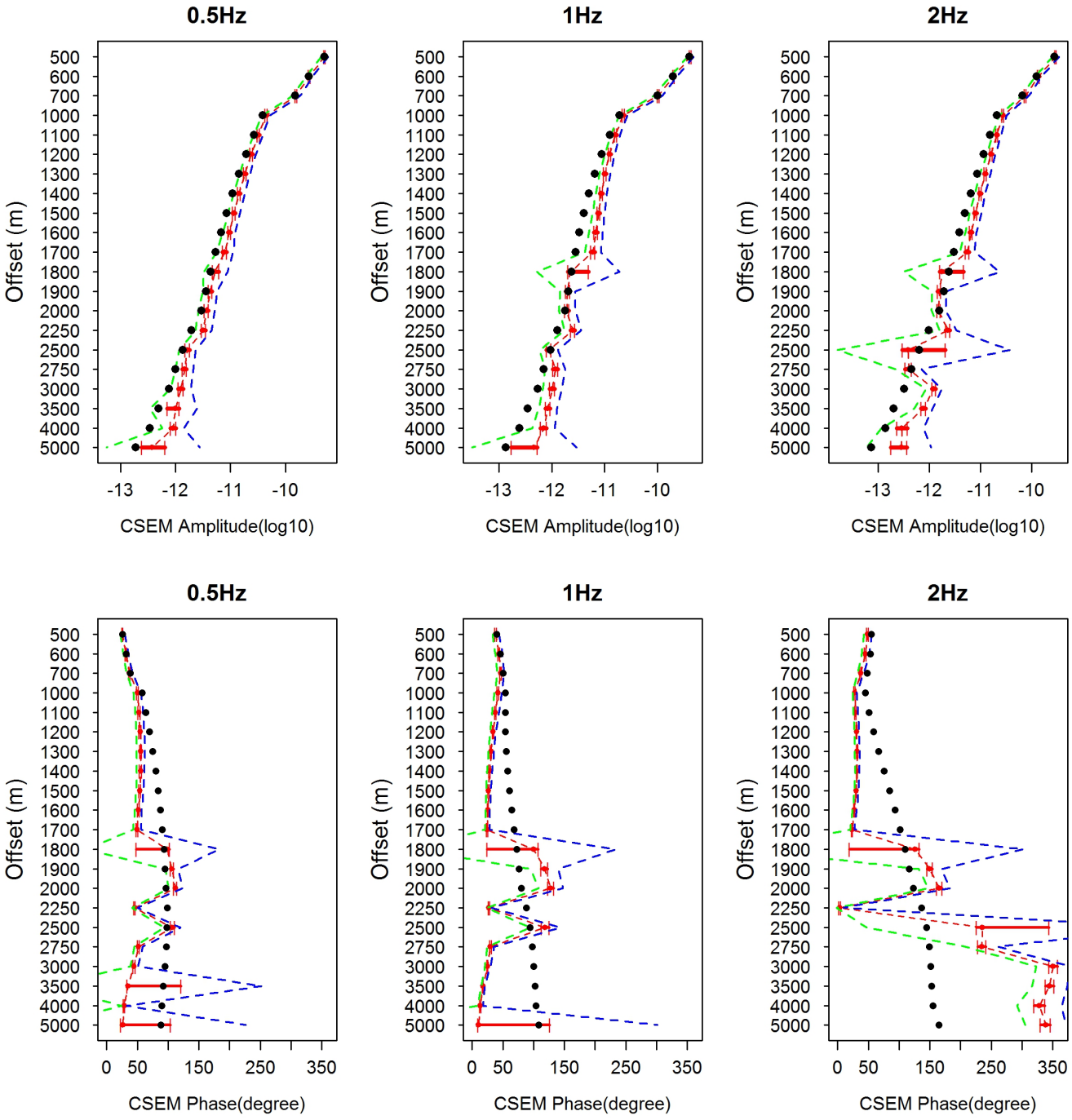
0.5Hz
1Hz
2Hz
Offset (m)
500
600
700
1000
1100
1200
1300
1400
1500
1600
1700
1800
1900
2000
2250
2500
2750
3000
3500
4000
5000
-13
-12
-11
-10
CSEM Amplitude(log10)
0
50
150
250
350
CSEM Phase(degree)

(b)

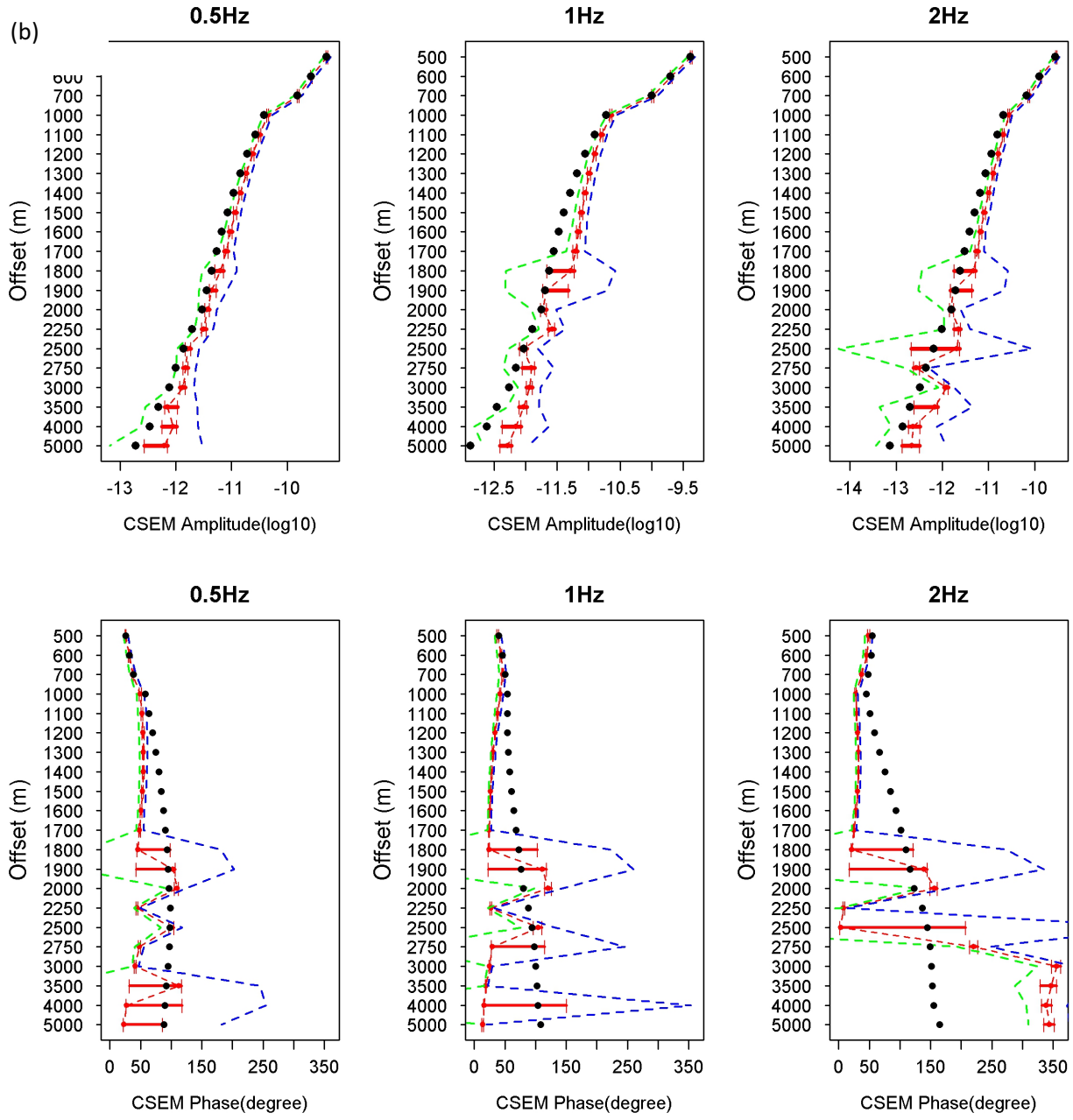
0.5Hz
1Hz
2Hz
Offset (m)
CSEM Amplitude(log10)
CSEM Phase(degree)

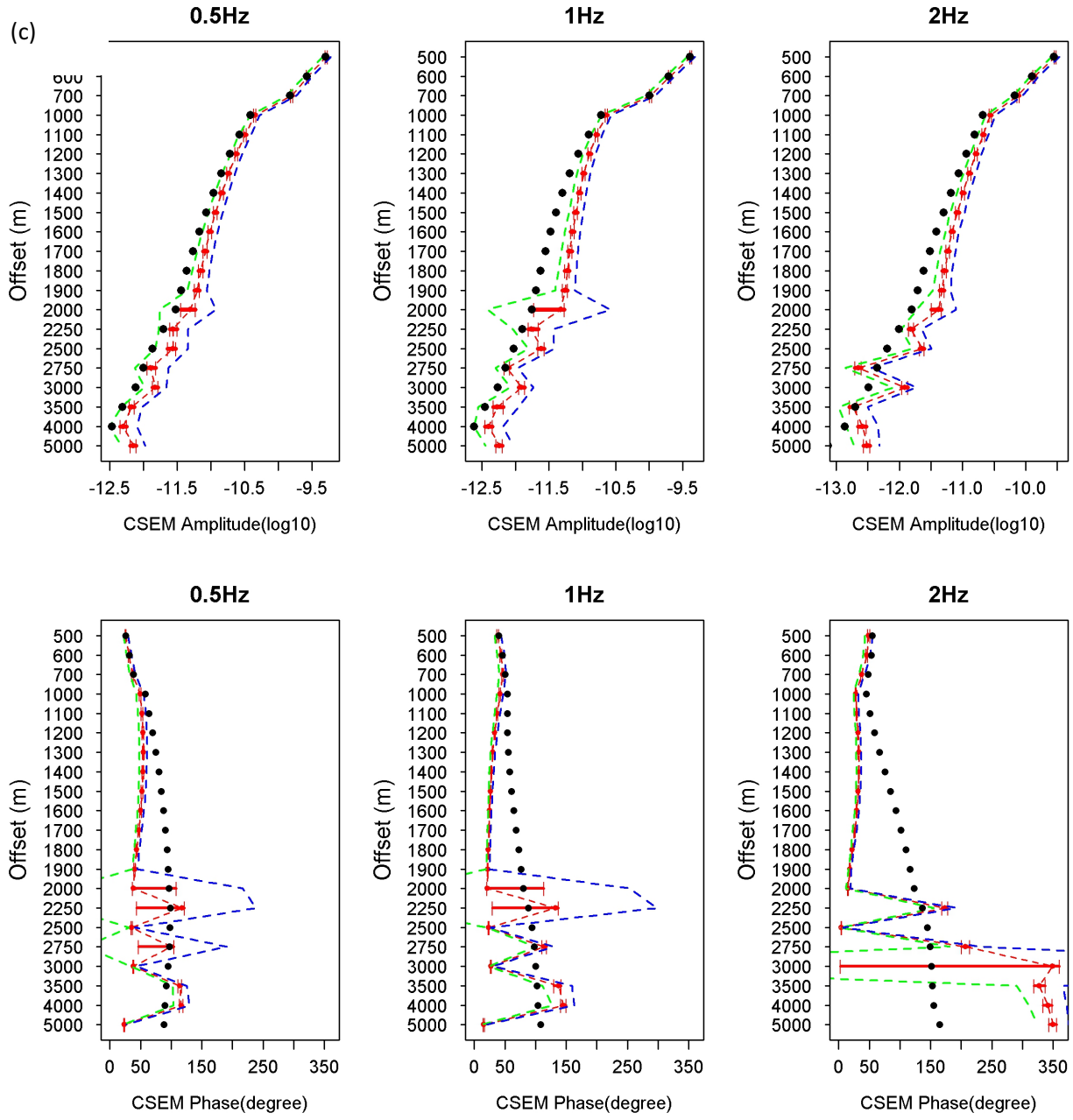
(c)
0.5Hz
1Hz
2Hz
Offset (m)
CSEM Amplitude(log10)
CSEM Phase(degree)

Figure 8.

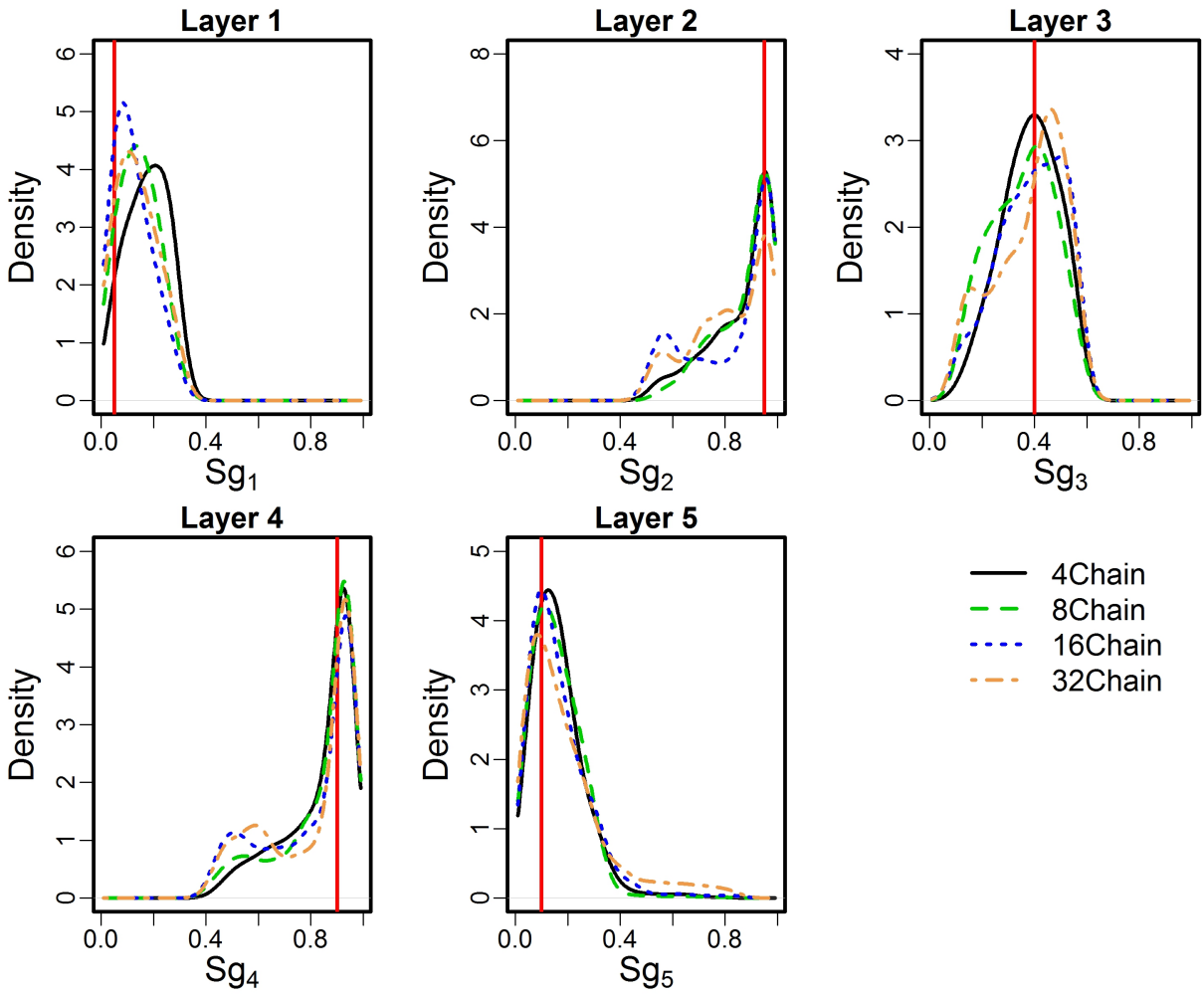
Layer 1
Layer 2
Layer 3
Layer 4
Layer 5
Density
Sg1
Sg2
Sg3
Sg4
Sg5
4Chain
8Chain
16Chain
32Chain

Figure 9.

Table

Table 1. The rock-physics model and Archie's law parameters used in the inversion.

Inversion domain (each layer)	Inversion domain thickness	50
	Pore pressure (GPa)	19.03
	Effective pressure(GPa)	5.84
	Temperature(ºC)	55
Reservoir(Rock-physics model parameters)	Grain shear pressure(GPa)	40.3278
	Grain Poisson ratio	0.05987
	Grain density(kg/m3)	2759.64
	critical porosity	0.37
	Number of grain contacts	11.7766
	Oil API gravity	59
	Gas gravity	0.03625
Archie's law coefficients	Archie's law constant	0.46426
	Water saturation exponent	-1.8646
	Porosity exponent	-1.3855

Table 2. The updated bounds of porosity for five layers obtained in seismic-only inversion.

	φ_1	φ_2	φ_3	φ_4	φ_5
True value	0.15	0.25	0.15	0.1	0.05
Narrow bounds	[0.129, 0.150]	[0.249, 0.289]	[0.139, 0.164]	[0.097, 0.117]	[0.029, 0.071]

Table 3. CRPS, MAE and dOF summaries of the seismic AVA observations and posterior predictions at various receivers in Fig. 7

Receiver	**R1 (0^o)**	**R2 (10^o)**	**R3 (20^o)**	**R4 (30^o)**	**R5 (40^o)**
CRPS	9.05e-04	2.12e-01	2.45e-02	5.39e-03	4.25e-01
MAE	2.60e-03	5.04e-01	6.20e-02	1.50e-02	1.13
d_{OF}	1.60e+01	2.2e+01	3.64e+01	1.96e+01	1.83e+01

Table 4. CRPS, MAE and dOF summaries of the CSEM phase observations and posterior predictions in Fig. 8 (top)

Frequency	**0.5 Hz**	**1 Hz**	**2 Hz**
CRPS	2.01e+01	3.48e+01	6.18e+01
MAE	2.55e+01	4.00e+01	7.33e+01
$\boldsymbol{d_{OF}}$	5.17e+02	8.60e+02	8.78e+02

Table 5. CRPS, MAE and dOF summaries of the CSEM amplitude observations and posterior predictions in Fig. 8 (bottom)

Frequency	**0.5 Hz**	**1 Hz**	**2 Hz**
CRPS	2.11e-12	2.04e-12	2.47e-12
MAE	3.91e-12	3.38e-12	3.55e-12
$\boldsymbol{d_{OF}}$	1.04e+02	1.35e+02	1.58e+02